Prediction of the grinding wheel specification influence on thermal defects in dry grinding through a hierarchical FEM model

Prediction of the grinding wheel specification influence on thermal defects in dry grinding through a hierarchical FEM model

Flavia Lerra[a*], Erica Liverani[a], Alessandro Ascari[a], Alessandro Fortunato[a]

a) University of Bologna, Viale Risorgimento 2, 40136 Bologna, Italy

Corresponding author: flavia.lerra2@unibo.it

Abstract

Grinding represents an indispensable phase in a manufacturing route because it allows to obtain the final required features in terms of dimensions and roughness. Although the grinding technology has always been applied with lubricants, nowadays, oil application becomes more and more limited to reduce the environmental pollution. In dry finishing technologies, heat control represents the main problematic of the process; indeed, grinding usually reaches relevant temperatures causing thermal defects. Therefore, process temperature prediction represents a challenge allowing to prevent thermal defects on the working material. But the final results are influenced by the kinematics parameters and also by the grinding wheel specifications. This paper aims to predict thermal defects in the material also considering the wheel specification. A hierarchical FEM model which considers both the microscopic and macroscopic aspects of the grinding process was developed. Starting from the mechanical action of a single grain on the material, a moving heat source was built to represent the interaction of the grinding wheel with the workpiece. A single grain grinding model is followed by a thermal model which considers the process parameters and the grinding wheel specification. Tangential grinding tests were developed to validate the model by adopting embedded thermocouples and grinding wheels with different structures were used. To further validate the model, metallographic and micro-hardness analyses were developed to verify the microstructural change due to the grinding cycle. A maximum average percentage difference of 10.8% was detected between calculated and measured temperatures and good agreement with the microstructural analysis was found.

Keywords**: Grinding burns; grinding wheel specification; FEM model**

1. Introduction

Grinding is an essential machining process usually adopted in the final steps of a manufacturing chain because it allows to obtain high-dimensional and surface quality requirements with the ability to finish difficult-to-cut materials. In general, lubricants are abundantly involved in grinding processes with the aim of reducing the heat generated during the removal action, but the reduction or the complete elimination of oil could lead to a decrease in production costs and promote a healthier manufacturing environment. At the same time, the oil absence enhance the thermal effects which are not only caused by inefficient cooling; indeed, they could also emerge from the wrong choose of the material removal rate, dressing operation, and the grinding strategy [1]. Beside conventional grinding, high-performance grinding processes, which use higher cutting speed and/or depths of cut with the aim to increase the productivity, have been investigated [2]. But an increase of the grinding parameters, such as the depth of cut, which represents the most influencing parameter on the grinding process, could easily cause thermal defects [3]. Therefore, due to the microstructural requirements, the grinding technology usually adopts low depth of cut. But, being the grinding a non-deterministic process due to the presence of undefined grain geometry, it could also generate high-specific energy values during the removal mechanism because of relevant deformation before the real cutting action. Indeed, the rubbing action, which starts at the initial stage of scratching, does not include plastic deformation and occurs within the elastic limit of materials, instead, the ploughing actions includes both elastic and plastic deformations and has significant influence on the process energy generation and the ground surface creation [4], [5]. Thermal effects are usually deleterious to surface integrity because they could lead to several defects due to a combination of mechanical and thermal loads [6]–[8]. With increasing process temperature thermal defects could be summarized in:

- chemical reactions leading to surface oxidation;
- grain growth, precipitation, and surface softening;
- phase transformations leading to surface re-hardening;
- thermal effects leading to expansion, contraction and possible cracking [9].

Therefore, grinding process especially without using lubricants could be considered as a thermal cycle where the heat absorbed by the material during the interaction with the tool could lead to a microstructural transformation. If excessive heat is generated, the workpiece may be damaged as thermal overloading leads to degradation of surface integrity and decrease of mechanical properties [10–12]. Low and normal heating rates are between 1 and 20 °C/s, high heating rates are between 20 and 100 °C/s, and ultra-fast heating rates are these above 100 °C/s [13]. The grinding technology could be identified as an ultra-fast heating process. Although values exist at thermodynamic equilibrium, for a given alloy composition, the critical temperatures are not unique for processing that deviates from equilibrium and depend on multiple factors including heating rate, cooling rate, and prior microstructure [14]. The steel critical temperature as a first attempt could be considered the starting austenitization temperature (723 °C), but it was demonstrated that in the ultra-fast heating processes, the critical temperature could slightly change, as reported in [36]. Therefore, the critical temperature related to a rapid heating process like grinding could slightly vary from the equilibrium conditions. Moreover, rapid austenitizing refines the austenite grain size if the initial microstructure is a fine aggregate [15], such as martensite leading to an increase in the mechanical properties but also in brittleness. Many models have been developed to predict the temperature reached during the

grinding phase and prevent the grinding burns, but several experimental tests are needed to achieve this challenging goal and the grinding wheel specification not always was considered. Most of the grinding models are based on the interaction of a moving heat source with the material starting from analytical consideration on the heat flux absorbed by the workpiece [16–20]. The maximum temperature rise is calculated through the heat flux generated by the removal mechanism, calculated as Eq.1:

$$(1)\ q_w = \frac{\varepsilon P}{l_c b}$$

where l_c and b are the contact arc length and width, P is the grinding power and ε the energy partition ratio. The grinding power represents the main contribution in calculating the heat fux and is usually measured experimentally, while the partition ratio represents the proportion of heat absorbed by the workpiece, and generally, it was defined by calibrating it through several experimental tests. Other authors based their analysis on different approaches, such as multinon-linear regression, response surface methodology, and Monte Carlo [21, 22], but the focus was mainly based on surface roughness prediction. Although a number of works were based on the grinding wheels' properties evaluation, only a few researchers have focused on the prediction of the thermal effect considering the specification of the wheel. Habrat analyzed the influence of the bond material in diamond wheels on cemented carbide by measuring the tangential and normal forces [23]. Zhao et al. investigated the effect of the pore structure and distribution on the flexural strength of porous Cu-Sn-Ti alumina composites showing that a larger pore size and a higher pores concentration reduce the composite strength, but it also provides more space for chip formation [24]. Gopan et al. developed a fast quantitative analysis of the grinding wheel loading using image processing [25]. Other approaches consider the grinding wheel properties starting from the single grain analysis. Zahedi et al. introduced the wheel topography starting from the single grain grinding simulation amplifying its effect through a probability distribution function to calculate the process forces [26]. Also, Tao introduced a normal distribution in his study to represent the grain size and position as random variables, but assuming the abrasive grains as spherical bodies [27]. Denkena et al. analyzed the grinding wheel manufacturing process and evaluated the mechanical interaction at grain/bond interface by means of scratch tests and forces measurements using a single grain tool [28, 29]. In this paper, a novel approach to predict grinding temperature and forecast thermal burns avoiding time-consuming power measurements and introducing the wheel specification was proposed. Micro- and macroscopic aspect of the grinding process were considered in a hierarchical combined model, which calculate the grinding forces and power generated by the mechanical action of a single grain and used this information to design a moving heat source that represent the interaction between a grinding wheel and the material in a thermal model. Single grain grinding tests and force measurements were previously performed to validate the first step of the model, then tangential grinding tests were performed using different grinding wheel and the process temperature were measured by means of embedded thermocouples to validate the model. Case-hardened steel typically used for automotive gears was used as workpiece material and fused aluminum oxide grinding wheel with FEPA size 60 and different specification were adopted and experimentally analyzed through an image processing approach to forecast the influence of porosity and binder during the grinding process. Microstructural and micro-hardness analysis were performed to verify the occurrence of thermal defects and to further validate the model.

2. Model description

The model is represented by a hierarchical FEM approach made up of a first step which analyses the mechanical action of a single grain on the material, followed by a second step which predicts the process temperature considering the interaction between the wheel and the material. The first part of the model is based on a microscopic approach and calculates the specific grinding power due to the removal material mechanism, instead, the second one analyses the macroscopic aspect of the process and, starting from the specific power output calculated from the previous phase, it predicts the process temperature by introducing a moving heat source in a thermal model. The single grain grinding model was validated through forces measurements by means of a dynamometer allowing to calculate an intermediate output represented by the single grain grinding power. The thermal model was directly validated through temperature measurements by means of embedded thermocouples and microstructural analysis. The main output of the model is represented by the process temperature reached during the grinding pass at the material surface, which give information about the thermal cycle and defects induced by the grinding process parameters. A combined analytical and experimental evaluation of the grinding wheel characteristics allows to introduce the wheel specification in the thermal model to verify also the influence of the wheel binder and structure. In Fig.1 the followed procedure was schematically shown.

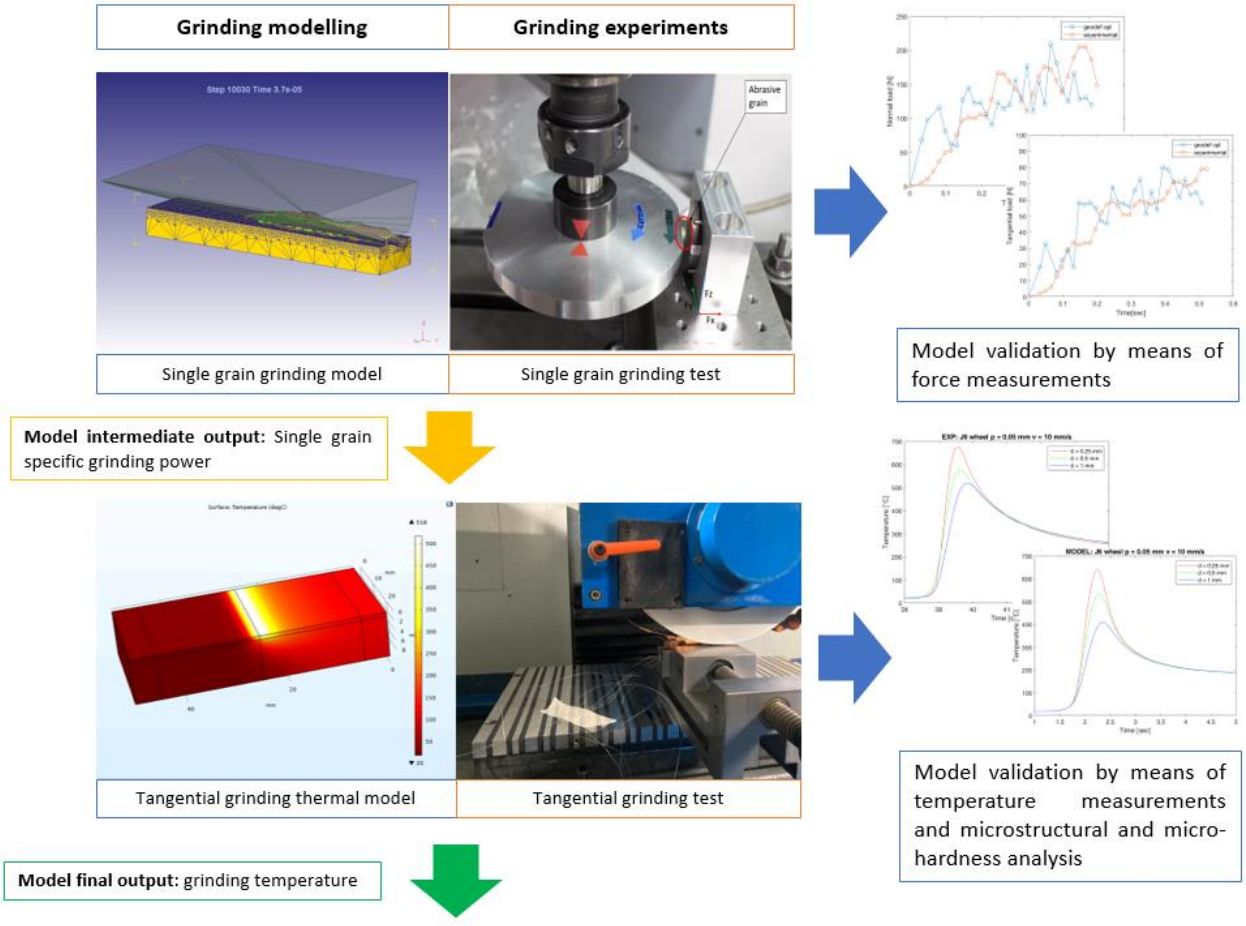

Fig. 1. Grinding thermal defects prediction modelling and experimental procedure

2.1. Single grain grinding model

In this section, a brief explanation of the frst step model was reported, but more details and results were presented in [30]. A mechanical FEM simulation was implemented in DEFORM-3D through a Lagrangian incremental approach. Dry contact conditions between the grain and the workpiece were simulated considering a constant Coulomb friction coefficient of 0.2 [31]. The grain was modelled as a rigid body being its hardness higher than the workpiece one. The workpiece was designed as a deformable prismatic body with dimensions allowing to reach the maximum depth of cut during the grain pass and was discretized with tetrahedral elements with fner dimensions near the contact zone so that the smallest element was equal to one-third of the cut depth. Translation and rotational movements were assigned to the grain to represent the real kinematics during experiments. Up-grinding was considered and zero velocity boundary conditions were applied to the lower workpiece surface to maintain its position fixed in the space. A time step of 100 ns was applied during the grain-workpiece interaction phase. Simulations adopted an equivalent defined grain geometry obtained through a real grain geometry simplification to reduce the computational costs. Real grain geometries were acquired by computed tomography and were elaborated to find the geometrical parameters characteristics of a size and material abrasive class (Fig. 2). In particular, the rake angle, the length, the width, and the tip radius were statistically considered as principal grain characteristics [32] to consider during the cutting process aiming to design a characteristic abrasive shape. Fused aluminum oxide was assigned as the grain material. For the workpiece material, the Johnson–Cook model, widely used to represent materials viscoplastic hardening and thermal softening with high strain-rate dependency, was employed to describe material flow according to Eq. (2).

$$\sigma = (A + B \cdot \varepsilon^{n}) \cdot (1 + \mathrm{C} \cdot \ln \frac{\dot{\varepsilon}}{\dot{\varepsilon_o}}) \cdot [\, 1 - (\frac{T - T_r}{T_m - T_r})^{m}] \qquad (2)$$

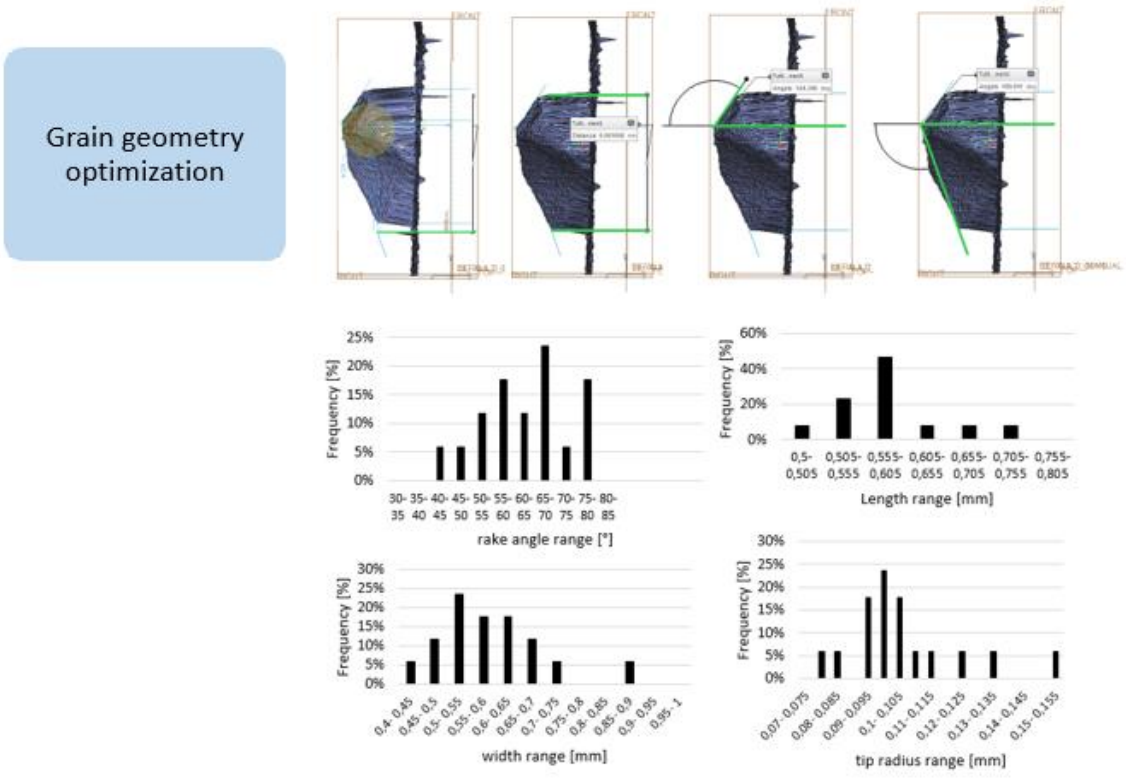

Fig. 2. Grain geometry analysis and optimization

where the parameter A is the initial yield strength of the material at room temperature, $\dot{\varepsilon}$ is the equivalent plastic strain rate normalized with a reference strain-rate $\dot{\varepsilon}$ e, *Tr* is the room temperature, *Tm* is the melting temperature of the material, and *B*, *C*, *n* and *m* are model parameters. The parameters *n*, *m* and *C* are the strain-hardening exponents, thermal softening exponent and strain-rate sensitivity, respectively. Optimized flow stress coefficients were adopted to represent the correct behavior of a case-hardened steel starting from a reference material mechanical flow stress curve. The J&C coefficients were determined through a characterization method based on Split Hopkinson pressure bar (SHPB) technology, which leads to characterize the reference material properties at high strain rates and high temperatures [33]. A flow stress calibration was implemented varying the coefficients A and B. In Fig. 3, the flow stress optimization procedure is shown. Coefficient A was varied over five levels from the reference value of 2480 MPa to−20%,−25%,−30%, and−35% of this value; instead, B was varied over three levels from the reference value of 1440 MPa to+20% and+30% of this value. A first simulation was used to calibrate the flow stress curve parameters and then was validated by simulating the single grinding test with different grain abrasives. In Tables 1 and 2, the most suitable flow stress coefficients for a case-hardened steel and the material properties were reported.

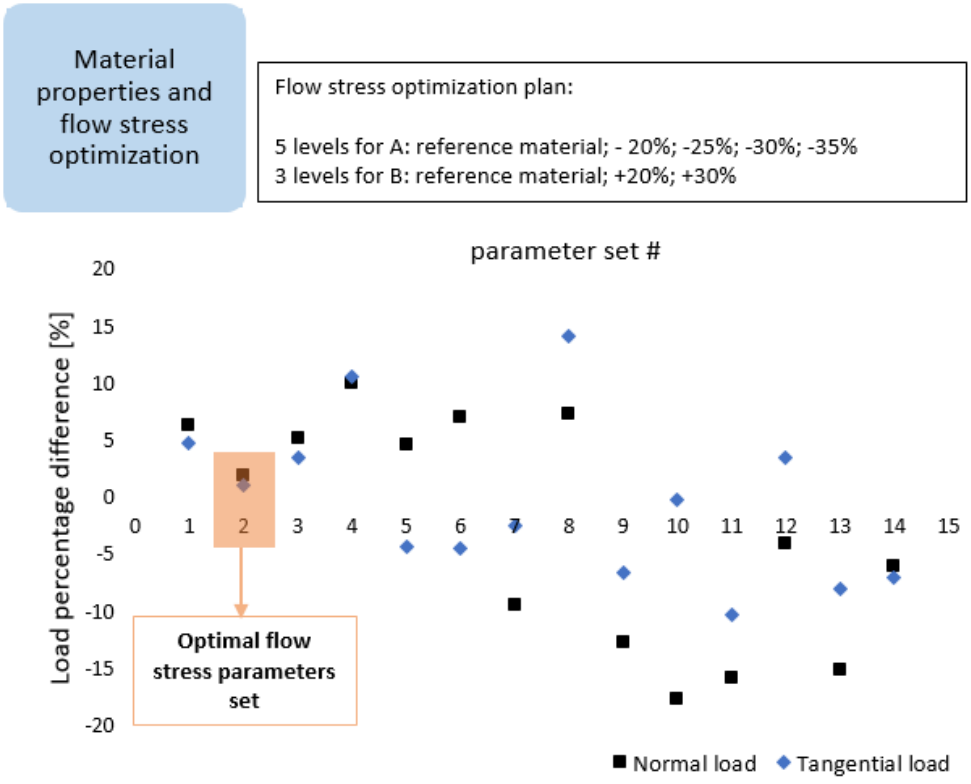

Fig. 3. Material flow stress curve analysis and optimization

Table 1. J&C parameters and material properties of reference material

J&C parameters	A	B	n	T_r	T_m	C	m
Ref. Material	2480	1440	0.45	20	1460	0.012	1.1

Table 2. Materials properties.

Material properties	ρ (kg/ m^3)	c_p (J/kgK)	λ (W/mK)	Hardness (HV1)
Workpiece	7850	354-916	24.57-24.75	750
Grain	3950	747-1106	6.10-23.71	2085

In Fig. 4, a resume of the single grain grinding model optimization is shown. An equivalent grain geometry definition and a calibration of the flow stress were introduced to develop and optimize the grinding microscopic model. The model validation was achieved through single grain grinding force acquisition using different abrasives with a maximum percentage difference of 12% [30]. After the single grain model validation, a simulation plan varying the depth of cut and feed rate was developed to calculate the grinding power within a defined parameters set. Since the grinding process in dry condition was considered, the hypothesis that all the grinding power generated during the removal mechanism was transformed into heat absorbed by the material was introduced.

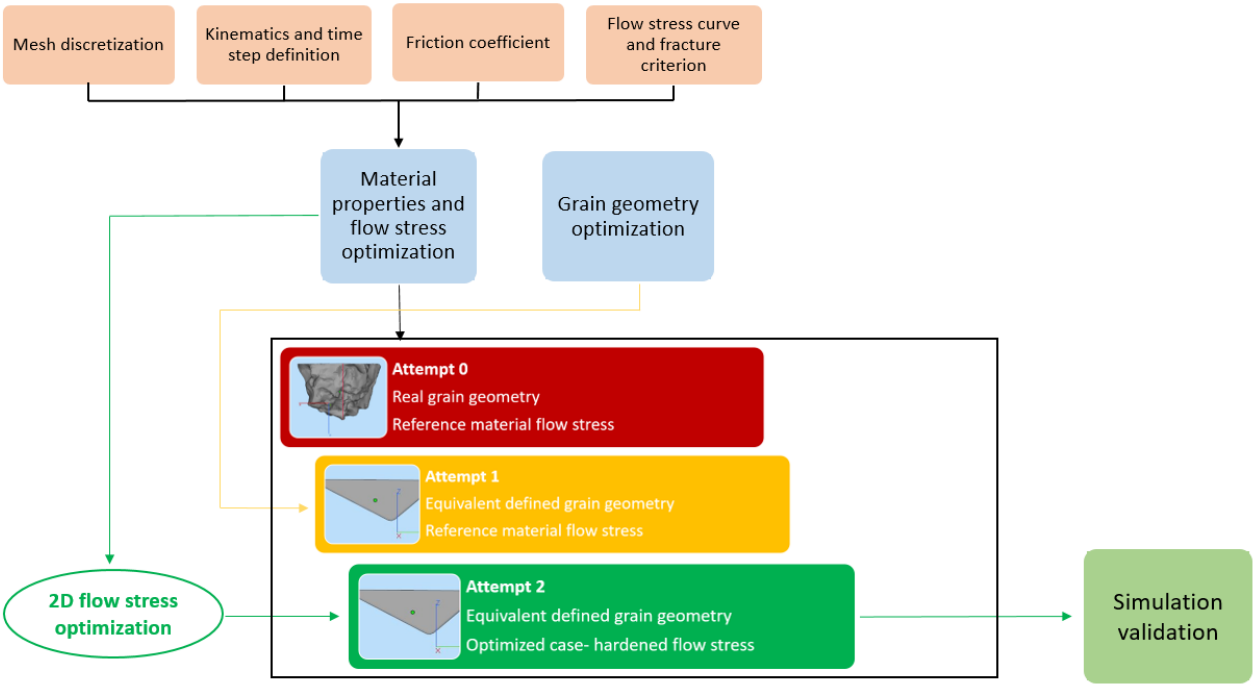

Fig. 4. Single grain grinding model optimization

2.2 Tangential grinding thermal model

The single grinding power calculation allowed to design the thermal contact between a cylindrical grinding wheel and the sample through a macro-scale FEM thermal model developed in COMSOL

MULTIPHYSICS version 5.4. The thermal model aimed to calculate and predict the process temperature generated during the actual grinding process. The thermal interaction between the material and the wheel was modelled as a moving heat source with a heat flux value distributed in the contact area directly derived from the single grain specific power calculation. The heat source assumed a translational speed equal to the feed rate value adopted during the tangential grinding tests and was characterized with a rectangular shape in x–y plane. The heat source dimensions are equal to the sample width and the theoretical contact length Lc calculated through Eq. (3), where Dw is the grinding wheel diameter and p the depth of cut.

$$Lc = \sqrt{p \cdot Dw} \quad (3)$$

The thermal cycle induced by the grinding is a rapid heating process, so that it could be approximated to a laser hardening process. Whereby, the heat source distribution was modelled with an asymmetrical top-hat intensity distribution in the y-z plane by means of an Erf function, as reported in Eq. (4), where *A* and *B* are the contact area dimensions and *a* and *b* define the rate of decrease in power density from the maximum value to zero [30].

$$\text{distr} = \frac{1}{4}\left[\text{Erf}\left(\frac{\text{A}-2\text{x}}{2\text{a}\sqrt{2}}\right) + \text{Erf}\left(\frac{\text{A}+2\text{x}}{2\text{a}\sqrt{2}}\right)\right] \cdot \left[\text{Erf}\left(\frac{\text{B}-2\text{y}}{2\text{b}\sqrt{2}}\right) + \text{Erf}\left(\frac{\text{B}+2\text{y}}{2\text{b}\sqrt{2}}\right)\right] \quad (4)$$

In this case, *a* and *b* were set equal to 0,1 and 0,6 respectively (Fig.5).

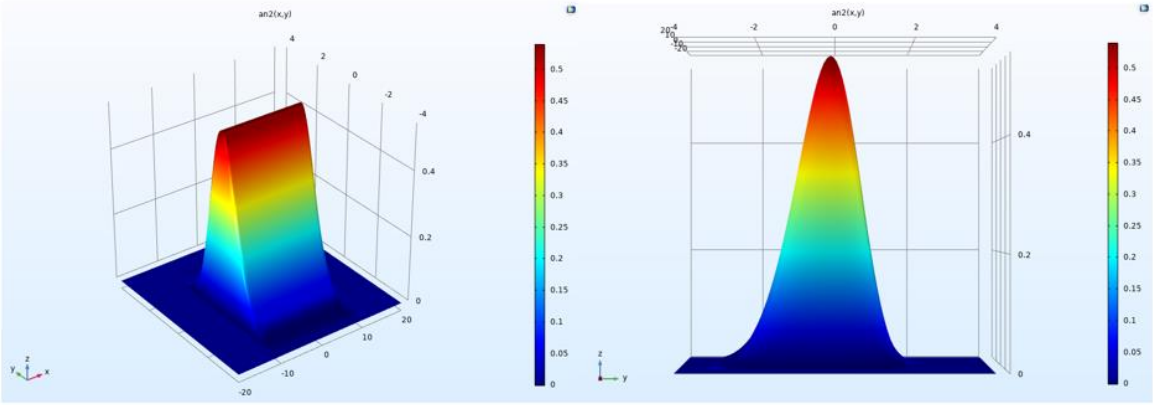

Fig. 5. Moving heat source definition for the tangential grinding thermal model

The heat source entity was modelled considering the average single grain grinding power obtained from the single grain grinding model. The power per grain *P*, which represent the heat generated by a single grain and absorbed by the material, was calculated by multiplying the single grinding power *Psg*, calculated with the single-grain model, with the grain–workpiece contact area *Ssgt* in the tangential direction calculated as the frontal contact area of a sphere having dimensions corresponding to the nominal mean abrasive grain size with the workpiece surface at the chosen depth of cut [30] and by dividing by the total contact area *Ssgn* in the normal direction determined by the kinematic process parameters set, as calculated through Eq. (5):

$$P = \frac{P_{sg} \cdot S_{sgt}}{S_{sgn}} \quad (5)$$

In Fig. 6 a representation of the before mentioned tangential and normal contact area was shown.

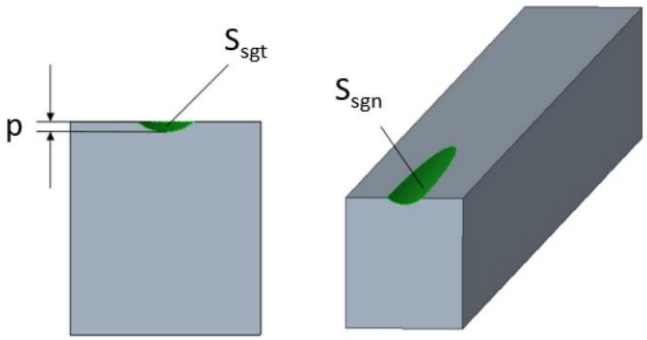

Fig. 6. Single grain tangential and normal contact area during the pass with a depth of cut p

The heat source entity was then obtained by multiplying the power per grain P with the specific number of grains n_g present in 1 mm^2, as reported in Eq. 6. In the following section, the procedure for the calculation of number of grains was explained.

$$I = P \cdot n_g \quad (6)$$

The assumption of considering the mean grain diameter derives from the fact that the most frequent grain size is the mean while the maximum and minimum grain sizes are rarely encountered [35]. The workpiece was discretized with free tetrahedral elements with a dimension of 250 µm in the surface depth and 1 mm in the bulk material. A constant time-step of 10 ms was implemented in (6) I = P · ng the model. The simulation plan was developed with the same process parameters according to the single grain grinding model and tangential experiments. A convection heat transfer coefficient of 15 W/m2 K was introduced. In Fig. 7, the moving heat source shape was reported as isothermal curve at the beginning, in the middle, and at the end of the grinding pass. Material assigned to the assembled sample was a casehardened steel, with a variation in the thermal conductivity law of the surface up to 1 mm in depth because of the martensite structure. Thermal conductivity values of the surface depth are reported in the Table 3 in function of the temperature [36]. Thermal probes were introduced at the beginning, in the middle, and at the end of the sample, as the real experiments, at a distance 0.25, 0.5, and 0.1 mm from the surface.

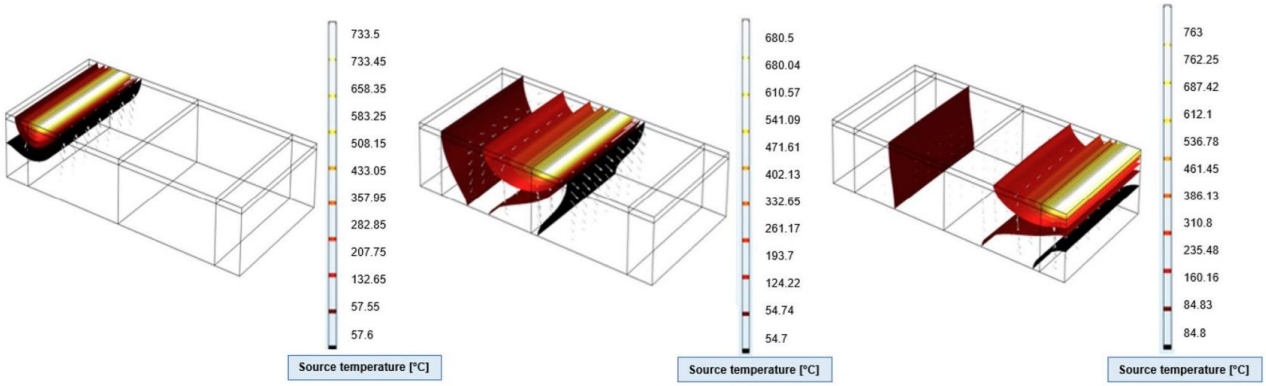

Fig. 7. Isothermal curve representing the moving heat source for the tangential grinding thermal model

Table 3. Martensite and austenite thermal conductivity varying with the temperature.

Temperature [°C]	0	300	600	800
Austenite thermal conductivity k [W/m K]	15	18	21.7	25.1
Martensite thermal conductivity k [W/m K]	43.1	36.7	30.1	

3. Experimental procedure

3.1. Grinding wheel specification analysis

The grinding wheel specification was introduced in the heat source design as grain density and was determined through a combined analytical and experimental evaluation. The average number of grains per mm^2 was calculated considering both the wheel porosity and the binder hardness. For the grains number calculation, the considerations reported in [25, 37] were resumed and adapted. The effective number of grains n_a which is involved in the grinding removal mechanism could be determined as a fraction φ_a of the approximated static grain quantity n.

$$n_a = \varphi_a n \quad (7)$$

The total number of static grains can be estimated starting from the volumetric concentration of abrasive grains in the wheel V_g through the following Eq. (8):

$$n = 6\, V_g \frac{l_c b}{\pi d_g^2} \quad (8)$$

Where d_g is the abrasive mean diameter that for a FEPA size of 60 is equal to 0.25 mm, l_c is the theoretical contact area and b is the workpiece sample. The volumetric concentration of abrasive grains V_g could be expressed through the following Eq. (9):

$$V_g = \frac{2\,(32-S)}{100} \quad (7)$$

Where S is the wheel structure number. For the calculation of the active grains number, the volumetric concentration of binder V_b and pores V_p were introduced as:

$$V_b = 1 - (V_g + V_p) \quad (10)$$

$$V_p = \frac{1}{100}\left(45 + \frac{S-2i}{1.5}\right) \quad (11)$$

Where i is an integer (i = 1, 2, 3, 4..) corresponding to the binder hardness letter (E,F,G,H..) respectively. The fraction of active grains φ_a can be determined by introducing a normalizing factor nf and a reference fraction coefficient φ_{ref}.

$$nf = 20{,}535\, V_b - 0{,}217 \quad (10)$$

$$\varphi_a = \varphi_{ref}\, nf \quad (11)$$

The reference fraction coefficient φ_{ref} is usually empirically determined in function of the wheel specification and considers the actual contacting grains during the pass. In this work, the reference fraction coefficient φ_{ref} was determined evaluating the grinding wheel specifications by means of image processing [38] using Matlab in order to have an experimentally verified indication of the

effective grains number that are, with high probability, in contact with the material. The grinding wheel was analyzed using a stereomicroscope Zeiss Stemi 508 evaluating samples of 1 mm2 of the total wheel area with a magnification of×2. Four different wheel specifications were analyzed: the porosity varied between 6, 9, and 12 structure number, representing an increasing porosity presence in the wheel. In particular, a porosity of 6 is related to a medium porosity value, porosity equal to 9 represents an open wheel, and 12 a porous wheel according to the standard designation system. Instead, the binder hardness chosen were J and H, so that a medium and softer wheel were tested. Ten acquisitions on all the wheel were performed. In Table 4 the grinding wheel specification were reported.

Table 4. Grinding wheel specification

Grinding wheel designation	Grain material	Grain size	structure	Binder hardness	Binder material
SG60 J6 VS3	Fused aluminum oxide	60	6 (medium)	J (medium)	Vitrified
SG60 J9 VS3	Fused aluminum oxide	60	9 (open)	J (medium)	Vitrified
SG60 J12 VS3	Fused aluminum oxide	60	12 (porous)	J (medium)	Vitrified
SG60 H9 VS3	Fused aluminum oxide	60	9 (open)	H (soft)	Vitrified

3.2. Grinding experimental tests

Single grain grinding tests were developed in dry conditions on a CNC tangential grinding machine. Cutting force components were measured using a Kistler 9255C dynamometer. Sintered aluminum oxide abrasive grains with a FEPA size of 60, representing medium abrasive grain dimensions, were used for the experiments, while case-hardened steel was employed as the workpiece material after heat treatment to achieve a hardness of 750 HV1 to a depth of at least 1 mm. Details of the single grain experimental tests were reported in [30]. Tangential grinding tests were performed on a CN Linea Iron 06.3 grinding machine using sintered aluminum oxide wheels with FEPA size 60 and different porosity. The experimental plan was performed in dry conditions adopting process parameters in accordance with the single grain grinding and thermal simulation plan. Process parameters adopted are shown in Table 5. Grinding wheel diameter was equal to 300 mm with a width of 50 mm, larger than the sample ground. Prismatic case-hardened steel samples with global dimensions of 20 × 50 × 15 mm were used for the experiments (Fig. 8). The specimens were previously case-hardened to reach a hardness of 750 HV1 in the surface layer up to 1 mm in depth as typical for gears heat treatment. On each sample, 9 grooves with a width of 1 mm were obtained for the thermocouples positioning. The thermocouples were positioned in three diferent sections of the sample: in correspondence of the beginning, the middle, and the end of the sample, in particular at 5, 25, and 45 mm from the starting edge of the the starting edge of the specimens to a different distance from the surface equal to 0.25, 0.5 and 1 mm.

Table 5. Tangential grinding tests process parameters

Cutting speed v_t [m/s]	Feed rate f [mm/s]	Depth of cut p [mm]	Grinding mode
20	10	0,01	Up-grinding
	20	0,025	
	40	0,05	

The overall sample was made up of four-part joint by screws. Thermocouple type k in Inconel with diameter of 0.25 mm and a maximum temperature acquisition of 1100 °C were used to measure the temperature during the grinding wheel pass. Each sample was ground with a total depth of cut of 0.1 mm every 3 µm before each grinding test to guarantee the surface planarity. The grinding wheel was dressed every three tests. Microstructural analysis and micro-hardness measurements were provided to verify the effect of the grinding process on the samples and validate the model. Microstructural analysis was carried out on each section in correspondence of the thermocouple position with an optical microscope Zeiss Axio Vert.A1M on the samples prepared according to standard metallographic techniques comprising mechanical grinding (80–2400 grit paper) and polishing with alumina in suspension down to a particle size of 1 µm. In order to reveal microstructural features, the samples were etched using Nital reagent for 3 s. Vickers micro-hardness tests were performed using a load of 1000 g for 20 s towards the hardened depth with indents spaced of 100 µm.

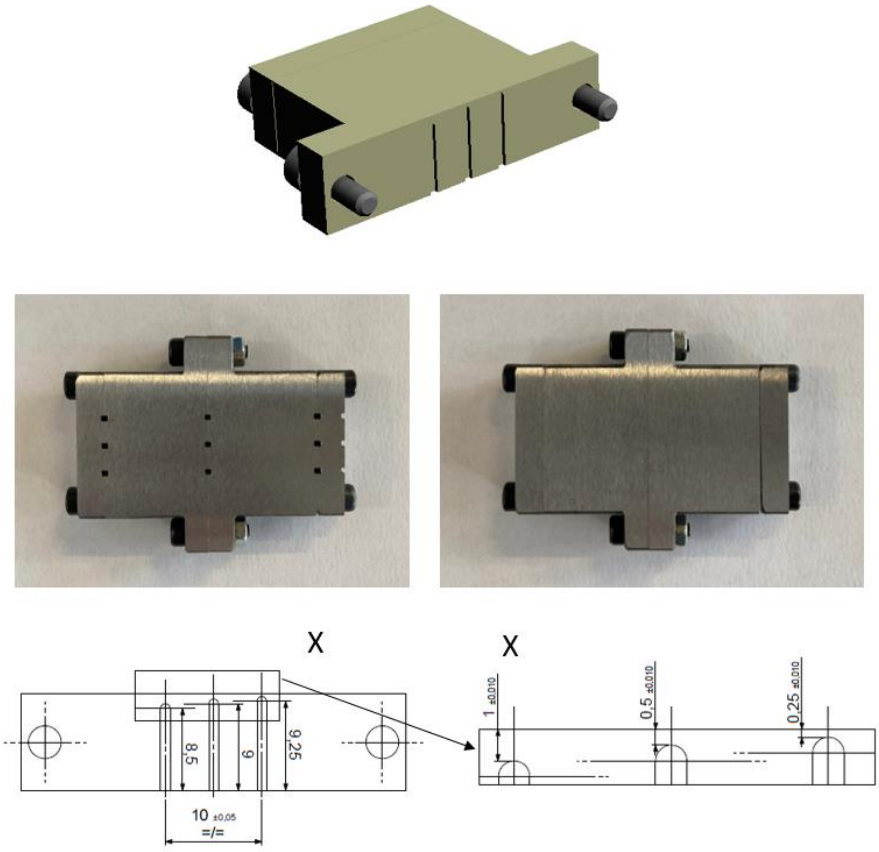

Fig. 8. Tangential grinding tests sample geometry

4. Results and discussion

This work aims to predict the grinding process temperature in dry conditions in order to prevent the thermal defect occurrence without performing several time-consuming experimental tests. A FEM hierarchical model was developed to avoid power measurements during the experimental tests; indeed, power generated during the grinding pass was calculated starting from a single grain grinding model which considers the mechanical contact between a single grain processed to represent a specifc material and size abrasive class. Single grain grinding validation and implementation were widely discussed in [30]. The model was applied to different abrasive geometries and then a simulation plan was developed to calculate the specific power in different process conditions. In Fig. 9, the single grain grinding power calculation was reported in function of the depth of cut and feed rate. The most influencing process parameter is represented by the depth of cut; indeed, a steep increase is visible increasing the cutting depth. The feed rate influence is lower in terms of single grain power generation; indeed, a negligible increase was reported increasing the feed rate values. The single grain power calculation was correlated with the grains density evaluation. An analytical approximation was developed to calculate a number of grains in contact with the material in a defined time step as a starting point, followed by an experimental visual inspection and the image processing of the wheel.

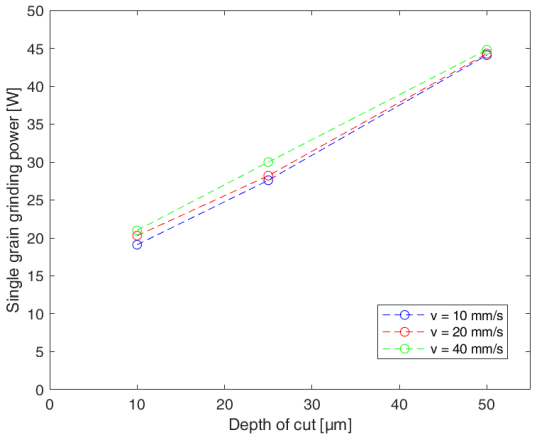

Fig. 9. Single grain grinding power calculation

In Fig. 10, an example of the acquisition of the wheel surfaces was reported and compared with the Matlab processed image results, showing an effective decreasing grain presence. Increasing the wheel porosity of one order, an average decrease of 5.5% in terms of grains number was detected. The grinding power was identified by the process parameters and the wheel number of grains per mm^2. In Fig. 11, the grain number per mm^2 evaluation was reported in function of the wheel specification. With the increase of porosity, the number of grains distributed in 1 mm2 decreases; therefore, an increase in porosity effectively reduces the grinding power contribution. Concerning the wheel binder hardness, it was indirectly identified by the number of grains because it is known that its influence affects the grain self-sharpening and not their distribution. Through the visual inspection, it was noticed that the grain density of the wheel with the softer binder was similar to that related to the grinding wheel with the same porosity. Through the approach proposed in this work, at equal structure, a decrease in binder hardness led to an apparent decrease of grain distribution on the wheel surface. Indeed, a softer binder reduces the grinding action in terms of thermal effect; therefore, this effect was identified with a decrease in the grinding heat source entity. The thermal effect of the different wheel specifications was reported in terms of temperature reached in the sample depth and surface microstructural transformation. The temperature was measured and calculated for all the

process parameter configurations and grinding wheel specifications. In Figs. 12, 13, 14, and 15, the comparison between the calculated and measured temperatures in the middle of the sample were reported for all the different wheel specifications in correspondence of a depth of cut of 0.05 mm and a feed rate of 10 mm/s being the thermal effect more visible. Model validation was achieved considering that the average percentage differences between the measured and calculated temperatures were detected equal to 4%, 9.8%, and 10.8%, respectively, for the thermocouples positioned at 0.25, 0.5, and 1 mm from the surface.

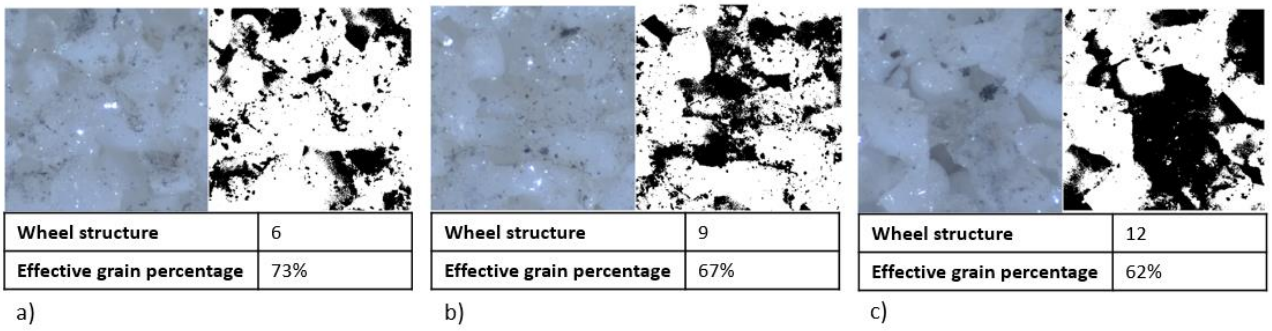

Fig. 10. Grinding wheel specification evaluation: structure a) 6; b) 9 and c) 12

Fig. 11. Grinding wheel grains density in function of the specification

Figures 12, 13, and 14 respectively show the comparison between calculated and measured temperature for the wheel SG60 J6 VS3, SG60 J9 VS3, and SG60 J12 VS3 with increasing porosity. Considering the temperature reached at the different surface depths, it was detected an average percentage difference in the measured temperatures of 33% between the less porous and the medium porous wheels, and a lower percentage difference between the medium porous and the more porous wheel equal to 9.5%. Comparing the thermal effect of the different wheel binder hardness, a substantial decrease of the dry grinding temperatures was detected with the softer wheel. Figures 13 and 15 report the temperature for the two different binder hardness results. A percentage reduction from the harder to the softer binder of 20.5%, 5.5%, and 4.5% was revealed in terms of process temperature respectively in correspondence of 0.25, 0.5, and 1 mm of distance from the surface.

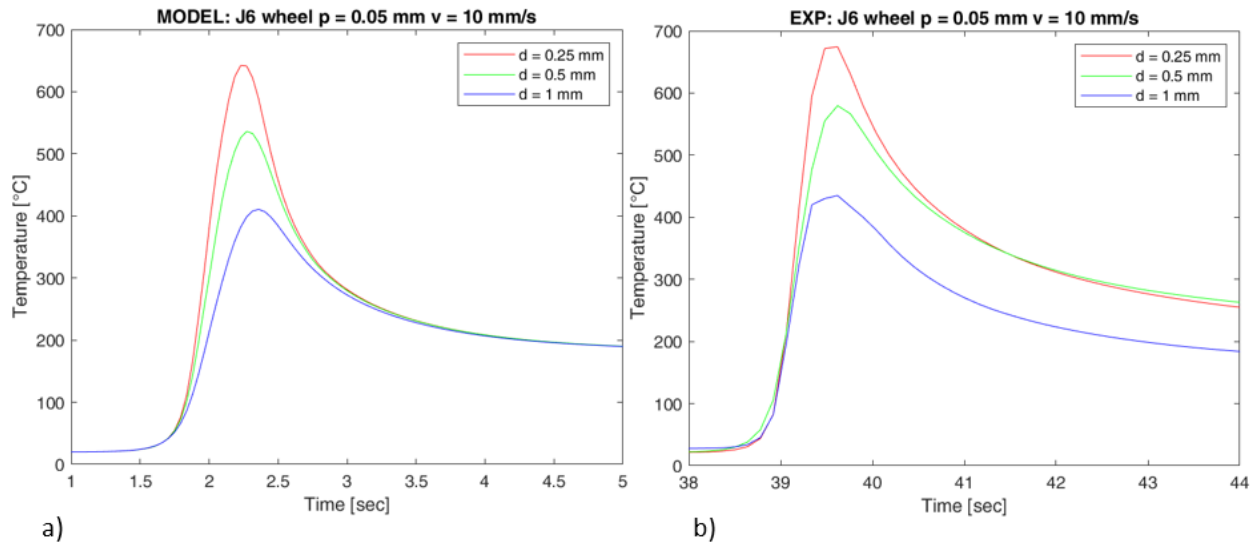

Fig. 12. Grinding temperatures comparison: a) calculated and b) measured temperatures at 0.25, 0.5 and 1 mm in depth in the middle of the sample with the SG60 J6 VS3 grinding wheel at v_t = 20 m/s; f = 10 mm/s; p = 0,05 mm

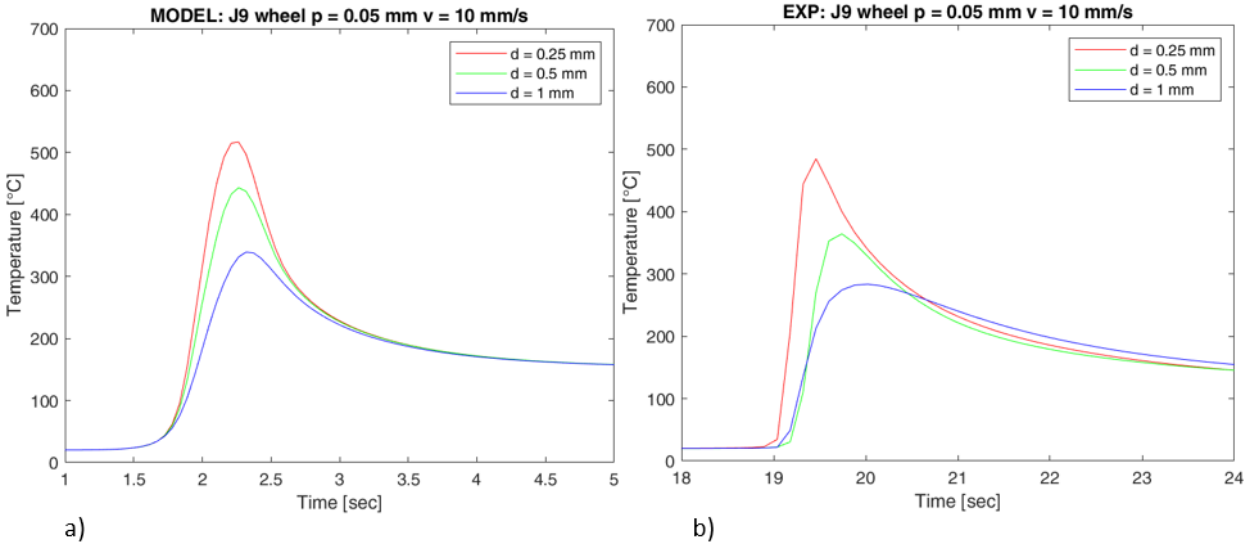

Fig. 13. Grinding temperatures comparison: a) calculated and b) measured temperatures at 0.25, 0.5 and 1 mm in depth in the middle of the sample with the SG60 J9 VS3 grinding wheel at v_t = 20 m/s; f = 10 mm/s; p = 0,05 mm

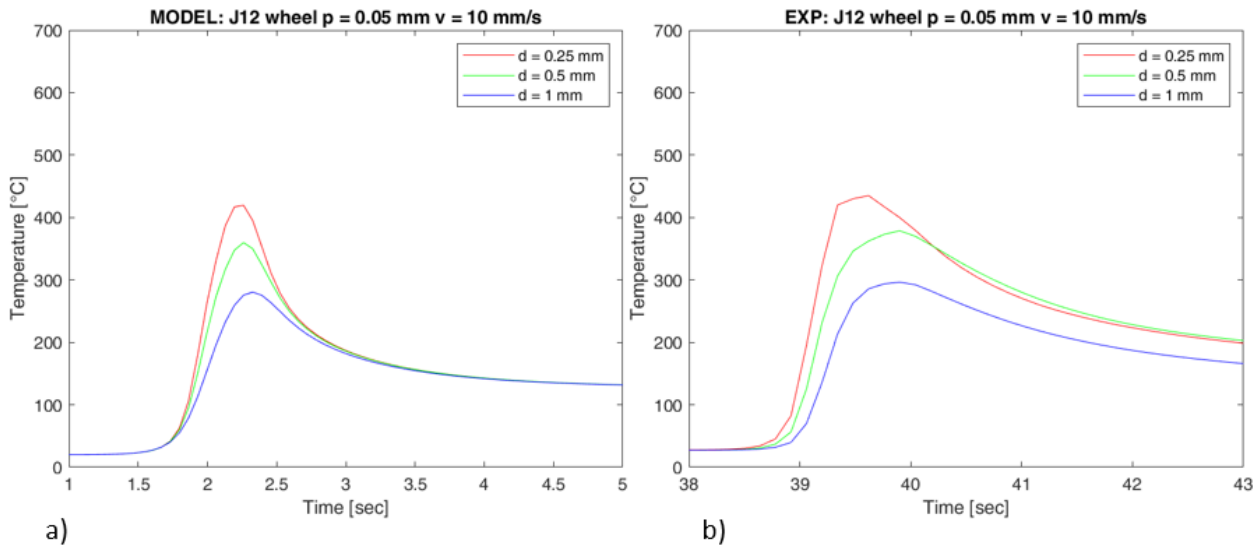

Fig. 14. Grinding temperatures comparison: a) calculated and b) measured temperatures at 0.25, 0.5 and 1 mm in depth in the middle of the sample with the SG60 J12 VS3 grinding wheel at v_t = 20 m/s; f = 10 mm/s; p = 0,05 mm

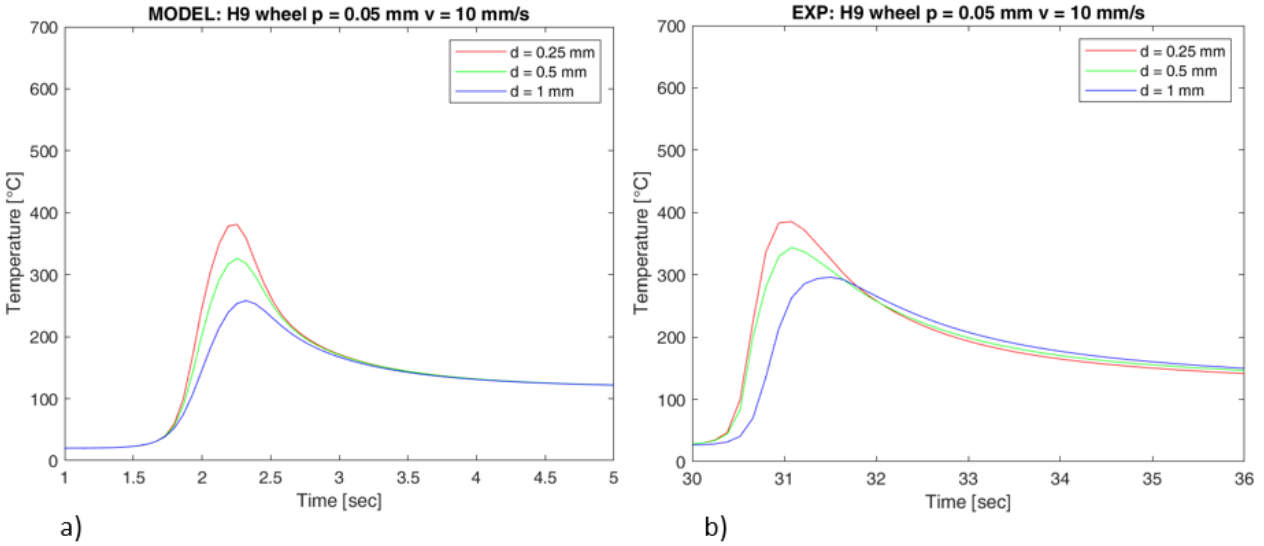

Fig. 15. Grinding temperatures comparison: a) calculated and b) measured temperatures at 0.25, 0.5 and 1 mm in depth in the middle of the sample with the SG60 H9 VS3 grinding wheel at v_t = 20 m/s; f = 10 mm/s; p = 0,05 mm

Maximum measured temperature was identified in correspondence of the less porous wheel SG60 J6 VS3 with a value of 675 °C. Increasing the porosity with the wheel specifications SG60 J9 VS3 and SG60 J12 VS3 the maximum temperatures measured at equal grinding conditions were 485 °C and 435 °C. Reducing the binder hardness from a grade J to H the maximum temperature measured at 0.25 mm from the surface was 385 °C with a reduction of 20%. According to the measured temperatures, it was verified that the heating and cooling process is very fast and overcomes the ultra-fast heating processes rates. From the measured temperature, it is visible that the maximum temperatures were reached in about 1 s, with a heating rate in the order of 100 °C/s. This effect was traduced in a thermal cycle on the surface material. In Fig. 16, the surface microstructures correlated with the temperature shown before were reported to show the effect of the different grinding wheel specifications adopted at equal process conditions. Microstructures shown were detected in

correspondence of a depth of cut of 0.05 mm and a feed rate of 10 mm/s. From the model, also the temperatures achieved at the surface were calculated; therefore, the validated model allows to consider the maximum temperatures reached within a defined process parameters set. of 771 °C, 741 °C, 493 °C, and 449 °C, respectively, for the three different structure and the softer binder. Temperatures calculated reflect the microstructural transformation reached in the dry ground material. Grinding thermal defects with the increasing process temperature occur in form of darkened and white layer. Further validation was represented by the micro-hardness measurements. The darkened layer is correlated to a softening effect of the surface, instead, the white layer brought to a surface re-hardening with a refinement of the grain size. This phenomenon often leads to an abnormal increase of the mechanical strength and crack formation.

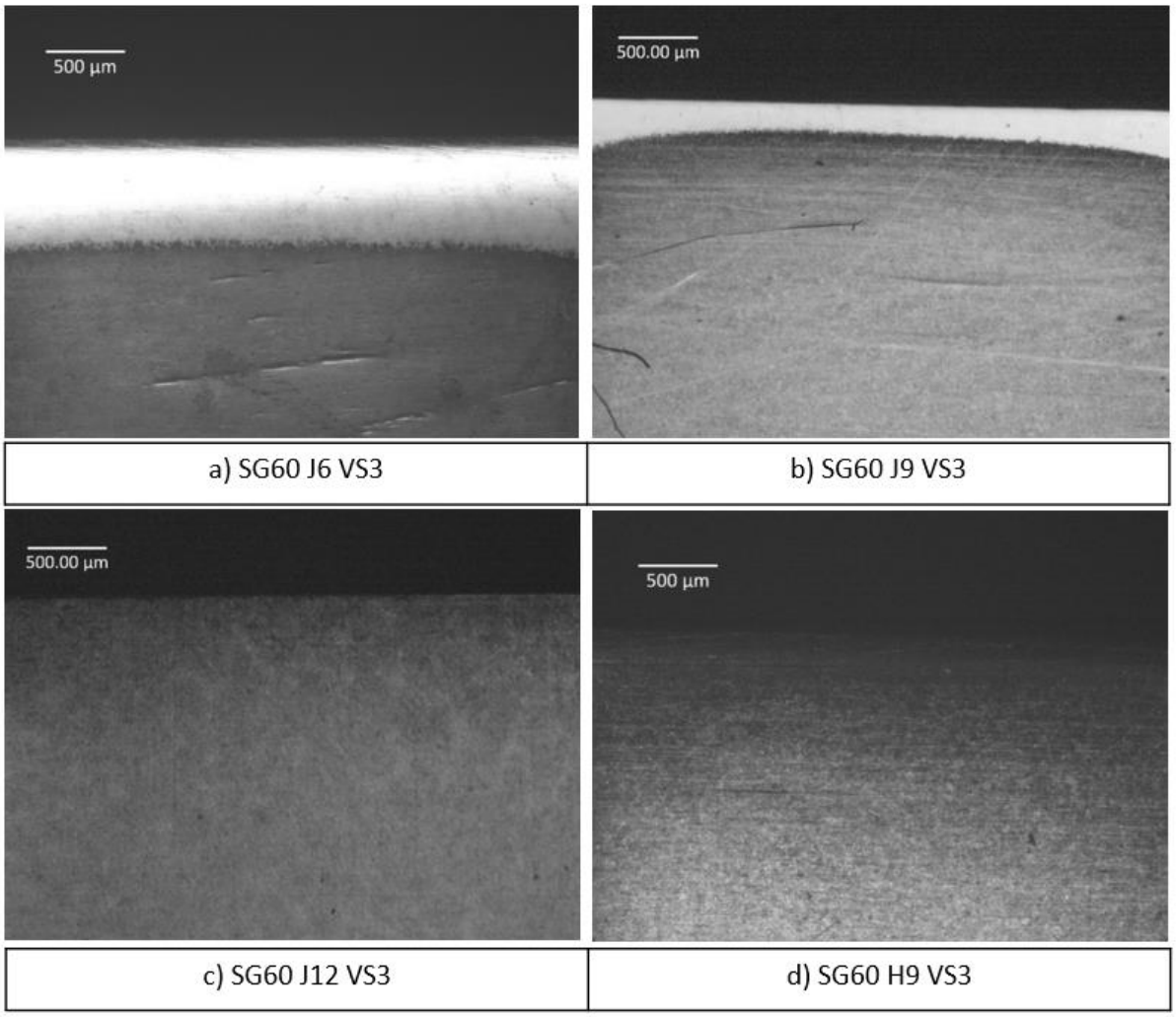

Fig. 16. Surface microstructural analysis comparison: a) SG60 J6 VS3 wheel; b) SG60 J9 VS3 wheel; c) SG60 J12 VS3 wheel and d) SG60 H9 VS3 wheel in correspondence of the middle of the sample with v_t = 20 m/s; f = 10 mm/s; p = 0,05 mm.

In Fig. 17, the micro-hardness measurements related to the microstructure reported are shown in comparison with the reference not ground material. The darkened layer occurred overcoming 400 °C; instead, the white layer appeared at temperatures higher than the austenitization temperature. According with the maximum grinding temperature reached, the microstructural analysis showed the occurrence of a white layer removing 0.05 mm at 10 mm/s with the wheel with low and medium porosity and a darkened layer with the higher structure and the softer binder. Comparing the surface micro-hardness of the reference material with the microstructure reached in the dry grinding

configurations considered, it was shown an increase of 16% of surface hardness with the low and medium porosity and a reduction of 25% and 37% respectively with the high porosity and softer binder wheel. Moreover, the micro-hardness showed a thicker hardened layer in correspondence of the low porosity wheel compared to the medium porosity wheel.

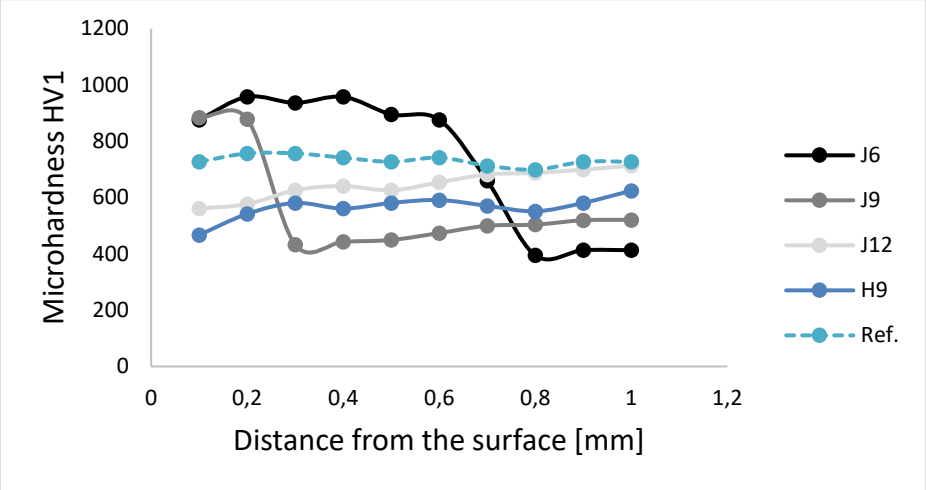

Fig. 17. Micro-hardness measurements comparison between the different grinding wheel specifications

The thermal effect of dry grinding is directly correlated with the wheel specifications; indeed, a low and medium porosity wheels, at equal process conditions, do not allow to remove heat enough during the material removal action and represent the worst conditions due to occurrence of white layers. High porosity wheel with harder binder gives a comparable effect of a wheel with medium porosity and softer binder because in both cases, a darkened layer appears with reduction of hardness. In this case, the effect of dry grinding is reduced compared to low and medium porosity wheels with harder binder, because an increase of porosity allows to dispose the heat generated grinding due to wider spaces between grains. The same effect is due to a softer binder that allows to easily remove worn grains.

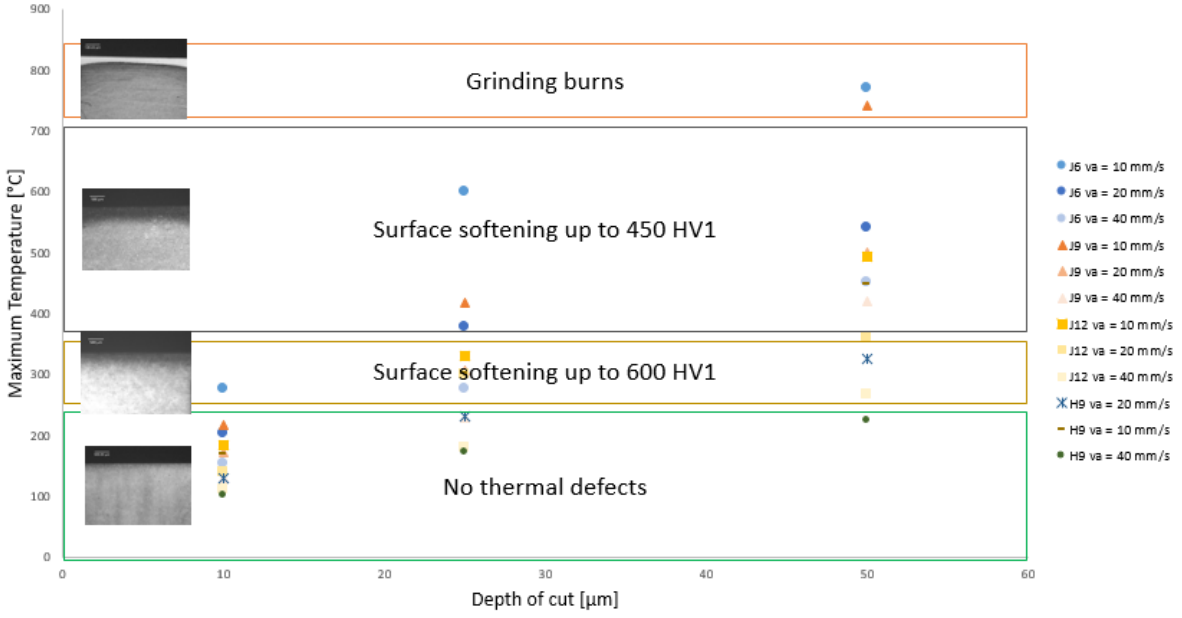

Fig. 18. Dry grinding maximum calculated temperatures and feasibility areas.

In Fig. 18, the maximum temperatures calculated by the model were reported for all the dry grinding configurations and grinding wheel adopted in the experimental plan. Increasing the depth of cut, the maximum temperatures increase because of the increase of the heat generated; instead, with an increase in feed rate, the interaction time between the wheel and material decrease and the maximum process temperature decrease. Grinding burns occur at the highest process temperature and start around the material austenitization temperature. With a decrease of the grinding heat generation, an area with a reduction of the hardness up to 450 HV1 was identified until 400 °C. Between 400 and 250 °C, an intermediate zone exists and it is characterized by a slightly decrease of the surface hardness up to 600 HV1. The feasibility area occurs under a maximum calculated temperature of 250 °C, where no defects were detected.

Conclusions

This work aimed to create and optimize a model able to predict thermal defects in a dry grinding process on casehardened material typically used in gears manufacturing. A hierarchical FEM model avoiding several time-consuming experimental power measurements was presented. A first single grain grinding model was implemented to calculate the grinding power generated during the interaction between a single grain and the material. The model was developed introducing an equivalent defined grain shape representative for the sintered aluminum oxide abrasive with size 60 and optimizing the flow stress behavior of the case-hardened material. A correlated following thermal model was developed to represent the interaction between the whole grinding wheel and the material in a tangential grinding process. A moving heat source was designed considering the wheel-material contact area and the wheel specification in terms of abrasive grains density. Three structures and two binder hardness were compared at equal grinding conditions to validate the model and show the different grinding wheel specification influence on the material. The thermal defect occurrence was predicted considering the temperature reached during the process and the model was validated by means of temperature measurements by adopting embedded thermocouples and through microstructural and micro-hardness analysis. The thermal effect of the grinding process is correlated to the moving heat source entity which was designed in function of the grain grinding power, the tangential and normal contact surfaces, and the abrasive grains density. Conclusions can be summarized in the following points:

- The single grain grinding power is directly dependent by the depth of cut and feed rate, but the cutting depth was detected being the most influencing kinematic grinding parameter;
- From a combined analytical and experimental evaluation of the grinding wheel specification it was identified a reducing grains density considering an increasing structure and a softer hardness binder.
- The model was validated considering that the average percentage differences between the measured and calculated temperatures was detected equal to 4%, 9.8% and 10.8% respectively for the thermocouples positioned at 0.25, 0.5 and 1 mm from the surface considering all the wheel specifications.
- Considering the grinding wheel specification effect, it was shown a reduction of the grinding temperature by increasing the porosity and using a softer binder. In particular, a decrease of 33% and 9.5% was detected between the low-medium porous wheels and medium-high porous wheels respectively. Instead, a maximum reduction of 20.5% was achieved by introducing a one grade softer binder hardness.

- Microstructural and micro-hardness measurements match with the maximum temperatures calculated. It was verified that a darkened layer occurs when a temperature about 400 °C was reached, instead, the white layer occurrence was detected overcoming the austenitization temperature of 723 °C.
- Comparing the surface micro-hardness of the reference material with the microstructure reached in the dry grinding tests, it was shown an increase of 16% of surface hardness with the low and medium porosity and a reduction of 25% and 37 % respectively with the high porosity and softer binder wheel.

References

[1] A. Fritsche and F. Bleicher, "Experimental investigation of the heat flux distribution in grinding of titanium alloy," *Procedia Eng.*, vol. 100, no. January, pp. 987–993, 2015, doi: 10.1016/j.proeng.2015.01.458.

[2] E. Procedure, "Surface Layer Properties of the," vol. 51, no. 1, pp. 105–108, 2012.

[3] G. Guerrini, F. Lerra, and A. Fortunato, "The effect of radial infeed on surface integrity in dry generating gear grinding for industrial production of automotive transmission gears," *J. Manuf. Process.*, 2019, doi: 10.1016/j.jmapro.2019.07.006.

[4] X. Chen, T. T. Opoz, and A. Oluwajobi, "Analysis of grinding surface creation by single-grit approach," *J. Manuf. Sci. Eng. Trans. ASME*, vol. 139, no. 12, pp. 1–10, 2017, doi: 10.1115/1.4037992.

[5] D. A. Doman, R. Bauer, and A. Warkentin, "Experimentally validated finite element model of the rubbing and ploughing phases in scratch tests," *Proc. Inst. Mech. Eng. Part B J. Eng. Manuf.*, vol. 223, no. 12, pp. 1519–1527, 2009, doi: 10.1243/09544054JEM1520.

[6] F. yuan Zhang, C. zheng Duan, M. jie Wang, and W. Sun, "White and dark layer formation mechanism in hard cutting of AISI52100 steel," *J. Manuf. Process.*, vol. 32, no. December 2017, pp. 878–887, 2018, doi: 10.1016/j.jmapro.2018.04.011.

[7] Z. Liao *et al.*, "Surface integrity in metal machining - Part I: Fundamentals of surface characteristics and formation mechanisms," *Int. J. Mach. Tools Manuf.*, vol. 162, no. December 2020, 2021, doi: 10.1016/j.ijmachtools.2020.103687.

[8] W. F. Sales, J. Schoop, L. R. R. da Silva, Á. R. Machado, and I. S. Jawahir, "A review of surface integrity in machining of hardened steels," *J. Manuf. Process.*, vol. 58, no. August, pp. 136–162, 2020, doi: 10.1016/j.jmapro.2020.07.040.

[9] W. B. Rowe and B. Dimitrov, *Tribology of Abrasive*. 2004.

[10] G. Guerrini, E. Landi, K. Peiffer, and A. Fortunato, "Dry grinding of gears for sustainable automotive transmission production," *J. Clean. Prod.*, vol. 176, pp. 76–88, 2018, doi: 10.1016/j.jclepro.2017.12.127.

[11] D. Sackmann, B. Karpuschewski, J. Epp, and R. Jedamski, "Detection of surface damages in ground spur gears by non-destructive micromagnetic methods," *Forsch. im Ingenieurwesen/Engineering Res.*, vol. 83, no. 3, pp. 563–570, 2019, doi: 10.1007/s10010-019-00368-z.

[12] J. E. Mayer, A. H. Price, G. K. Purushothaman, A. K. Dhayalan, and M. S. Pepi, "Specific grinding energy causing thermal damage in helicopter gear steel," *J. Manuf. Process.*, vol. 4,

no. 2, pp. 142–147, 2002, doi: 10.1016/S1526-6125(02)70140-0.

[13] S. Papaefthymiou, A. Banis, M. Bouzouni, and R. H. Petrov, “Effect of ultra-fast heat treatment on the subsequent formation of mixed martensitic/bainitic microstructure with carbides in a crmo medium carbon steel,” *Metals (Basel).*, vol. 9, no. 3, 2019, doi: 10.3390/met9030312.

[14] D. K. Matlock, S. Kang, E. De Moor, and J. G. Speer, “Applications of rapid thermal processing to advanced high strength sheet steel developments,” *Mater. Charact.*, vol. 166, no. February, p. 110397, 2020, doi: 10.1016/j.matchar.2020.110397.

[15] R. A. Grange, “The rapid heat treatment of steel,” *Metall. Trans.*, vol. 2, no. 1, pp. 65–78, 1971, doi: 10.1007/BF02662639.

[16] S. Malkin and C. Guo, “Thermal Analysis of Grinding,” *CIRP Ann. - Manuf. Technol.*, vol. 56, no. 2, pp. 760–782, 2007, doi: 10.1016/j.cirp.2007.10.005.

[17] T. Jin and D. J. Stephenson, “Three dimensional finite element simulation of transient heat transfer in high efficiency deep grinding,” *CIRP Ann. - Manuf. Technol.*, vol. 53, no. 1, pp. 259–262, 2004, doi: 10.1016/S0007-8506(07)60693-3.

[18] J. Zhang, H. Xu, Y. Yu, and Z. Wei, “FEM based numerical analysis on the temperature field in grind-hardening,” *CIS 2009 - 2009 Int. Conf. Comput. Intell. Secur.*, vol. 1, no. 1, pp. 615–618, 2009, doi: 10.1109/CIS.2009.207.

[19] D. Anderson, A. Warkentin, and R. Bauer, “Experimental validation of numerical thermal models for dry grinding,” *J. Mater. Process. Technol.*, vol. 204, no. 1–3, pp. 269–278, 2008, doi: 10.1016/j.jmatprotec.2007.11.080.

[20] A. G. Mamalis, J. Kundrák, D. E. Manolakos, K. Gyáni, and A. Markopoulos, “Thermal Modelling of Surface Grinding Using Implicit Finite Element Techniques,” *Int. J. Adv. Manuf. Technol.*, vol. 21, no. 12, pp. 929–934, 2003, doi: 10.1007/s00170-002-1410-3.

[21] W. F. Habrat, “Effect of bond type and process parameters on grinding force components in grinding of cemented carbide,” *Procedia Eng.*, vol. 149, no. June, pp. 122–129, 2016, doi: 10.1016/j.proeng.2016.06.646.

[22] B. ZHAO, T. YU, W. DING, and X. LI, “Effects of pore structure and distribution on strength of porous Cu-Sn-Ti alumina composites,” *Chinese J. Aeronaut.*, vol. 30, no. 6, pp. 2004–2015, 2017, doi: 10.1016/j.cja.2017.08.008.

[23] V. Gopan and K. L. D. Wins, “Quantitative Analysis of Grinding Wheel Loading Using Image Processing,” *Procedia Technol.*, vol. 25, no. Raerest, pp. 885–891, 2016, doi: 10.1016/j.protcy.2016.08.198.

[24] A. Zahedi and B. Azarhoushang, “FEM Based Modeling of Cylindrical Grinding Process Incorporating Wheel Topography Measurement,” *Procedia CIRP*, vol. 46, pp. 201–204, 2016, doi: 10.1016/j.procir.2016.03.179.

[25] B. Denkena, A. Bouabid, and A. Kroedel, “Single grain grinding: a novel approach to model the interactions at the grain/bond interface during grinding,” *Int. J. Adv. Manuf. Technol.*, vol. 107, no. 11–12, pp. 4811–4822, 2020, doi: 10.1007/s00170-020-05219-8.

[26] F. Kempf, A. Bouabid, P. Dzierzawa, and B. Denkena, “Methods for the analysis of grinding wheel properties,” pp. 87–96.

[27] F. Lerra, E. Liverani, E. Landi, and A. Fortunato, “Real single grain grinding FEM

simulation for case-hardened steel based on equivalent contact area analysis," *J. Manuf. Sci. Eng.*, pp. 1–24, 2021, doi: 10.1115/1.4051536.

[28] G. Q. Cai, B. F. Feng, T. Jin, and Y. D. Gong, "Study on the friction coefficient in grinding," *J. Mater. Process. Technol.*, vol. 129, no. 1–3, pp. 25–29, 2002, doi: 10.1016/S0924-0136(02)00569-1.

[29] F. Klocke, C. Wrobel, M. Rasim, and P. Mattfeld, "Approach of Characterization of the Grinding Wheel Topography as a Contribution to the Energy Modelling of Grinding Processes," *Procedia CIRP*, vol. 46, pp. 631–635, 2016, doi: 10.1016/j.procir.2016.04.011.

[30] G. Guerrini, A. H. A. Lutey, S. N. Melkote, A. Ascari, and A. Fortunato, "Dry generating gear grinding: Hierarchical two-step finite element model for process optimization," *J. Manuf. Sci. Eng. Trans. ASME*, vol. 141, no. 6, pp. 1–9, 2019, doi: 10.1115/1.4043309.

[31] Z. B. Hou and R. Komanduri, "On the mechanics of the grinding process - Part I. Stochastic nature of the grinding process," *Int. J. Mach. Tools Manuf.*, vol. 43, no. 15, pp. 1579–1593, 2003, doi: 10.1016/S0890-6955(03)00186-X.

[32] A. Sue and G. Schajer, *Material Factors - Handbook of residual stressand deformation of steel*. 2002.

[33] K. Salonitis, P. Stavropoulos, and A. Kolios, "External grind-hardening forces modelling and experimentation," *Int. J. Adv. Manuf. Technol.*, vol. 70, no. 1–4, pp. 523–530, 2014, doi: 10.1007/s00170-013-5260-y.

[34] K. Salonitis, T. Chondros, and G. Chryssolouris, "Grinding wheel effect in the grind-hardening process," *Int. J. Adv. Manuf. Technol.*, vol. 38, no. 1–2, pp. 48–58, 2008, doi: 10.1007/s00170-007-1078-9.

[35] V. Gopan and K. L. D. Wins, "Quantitative Analysis of Grinding Wheel Loading Using Image Processing," *Procedia Technol.*, vol. 25, no. Raerest, pp. 885–891, 2016, doi: 10.1016/j.protcy.2016.08.198.

[36] E. Liverani, D. Sorgente, A. Ascari, L. D. Scintilla, G. Palumbo, and A. Fortunato, "Development of a model for the simulation of laser surface heat treatments with use of a physical simulator," *J. Manuf. Process.*, vol. 26, pp. 262–268, 2017, doi: 10.1016/j.jmapro.2017.02.023.